Electronic Supporting Information

3D to 2D reorganization of silver-thiol nanostructures, triggered by solvent vapor annealing

Simone Dell'Elce, Fabiola Liscio, Alessandro Kovtun, Stefano Allegri, Otello M. Roscioni, Cristiano Albonetti, Giovanna De Luca, Heinz W. Amenitsch, Nicola Demitri, Loris Giorgini, Vittorio Morandi, Francesco Stellacci, Andrea Liscio*, Vincenzo Palermo

Measurement of Size dispersity index (D$_R$)

We used AFM to measure the average size and size distribution (i.e. the dispersity) of several hundreds of IBANs deposited on Si substrates at low concentration to avoid NP aggregation. Using an AFM image of IBAN deposited on ultra-flat substrate with low concentration, as depicted in fig. S1, it is possible to distinguish unambiguously the isolated nanoparticles from the surrounding substrate and as well as to calculate the size histogram $f(R_i)$ using standard image analysis software (SPIP from Image Metrology and Gwyddion by Czech Metrology Institute).

$f(R_i)$ is the number of measured objects having a given radius (R_i), so that $\sum_i f(R_i) = N$, i.e. the total number of particles counted.
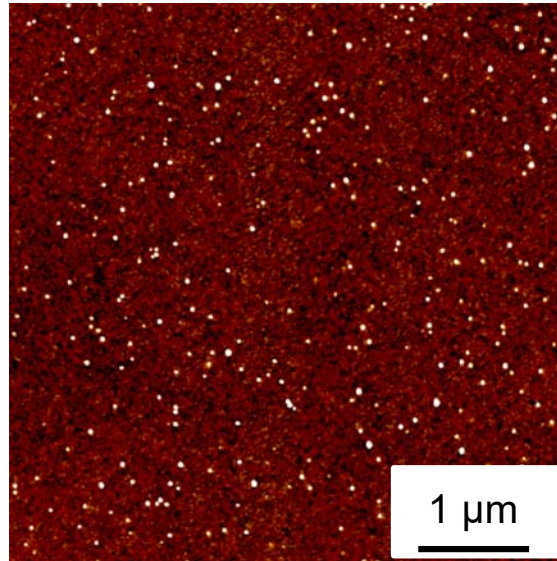

Figure S1. AFM image of IBANs deposited from DMF solution native silicon oxide substrate. Z range = 2 nm.

We define the discrete distribution (p_i) and the corresponding momenta $\langle R^\alpha \rangle$ as:

$$p_i = \frac{f(R_i)}{N} \quad \text{and} \quad \langle R^\alpha \rangle = \sum_i R_i^\alpha \cdot p_i \tag{S1}$$

where $\langle ... \rangle$ indicates the expectation value of the moment of order α of the size discrete distribution.

Among these moments, the most important ones are of order one ($\alpha=1$) and two ($\alpha=2$).

$\alpha=1$ corresponds to the average radius $\langle R \rangle$ and $\alpha=2$ to the average of the radius squared $\langle R^2 \rangle$.

Dispersity is a measure of the heterogeneity of sizes of particles. Thus, we defined the size dispersity index (D_R) in terms of momentum distributions:

$$D_R = \langle R^2 \rangle / \langle R \rangle^2 \qquad\qquad (S2)$$

In the case of monodispersed objects, D_R is equal to the unit. In real samples, the higher the value, the larger the radius distribution.

AFM images were studied using an automatic image processing analysis performed on >600 NP. The analysis yielded an average radius of 15±8 Å and a $D_R = 1.2\pm0.3$, which is comparable to the value expected for monodispersed objects ($D_R = 1$).

The measured D_R is intrinsically higher than 1 because of the noise level of the AFM measurements and the finite size of the tip ($R_{tip} \gtrsim R_{IBAN}$).

Optical absorption and scattering measurements

UV-vis absorption spectra

We monitored IBANs in different solvents by measuring the absorption spectra (A_t) in the first 24 hours. To this aim, we performed a quantitative analysis of the changes in spectrum intensity and line shape, as described below.

In general, spectra can change the absolute values $<A>$ and as well as the line-shapes, a.k.a. the relative intensities (Δ_{shape}), defined respectively as:

$$\langle A \rangle = \frac{1}{N}\sum_i A_i \tag{S3a}$$

as the mean value of the measured UV-vis absorption spectrum, N is the number of experimental data acquired at different wavelength;

$$\Delta_{shape} = (\tilde{A}_t - \tilde{A}_0)/\tilde{A}_0 \times 100\% \text{ , where } \tilde{A} = A/\langle A \rangle \tag{S3b}$$

which is the percentage relative variation respect to the pristine solution at 0h (A_0).

The time-dependence of the line-shape provides direct information on the IBAN stability in solution.

In the case of complete stability: $\Delta_{shape} = 0$, the equation S3 can be written as:

$$\frac{A_t}{A_0} = \frac{\langle A_t \rangle}{\langle A_0 \rangle} = constant \tag{S4}$$

This condition is satisfied in two cases:

$$A_t = A_0 \tag{S5a}$$

$$A_t/\langle A_t \rangle = A_0/\langle A_0 \rangle = constant \tag{S5b}$$

The first is the obvious case: the absorption spectra do not change in time and, thus, IBANs are stable in solution.

In the second case, the equality reported in S4 is satisfied when each point of the A spectrum changes as the corresponding mean value. In this case, the absolute intensity can vary but the line-shape of the spectrum is constant.

The latter case corresponds to the case in which the chemical-physical properties of the single scattering centers do not change (i.e. the line-shape is constant) unlike the intensities which typically decreases due to the variation of the nanoparticle concentration in solution due to the precipitation.

In general, the closer the Δ_{shape} to 0 the higher the solution stability.

The Absorption spectra of IBANs in acetone and DCM are shown in main text. The spectra of IBAN in DMF is reported in fig. S2, showing a much better stability of IBAN in this solvent, as compared to acetone and DCM.
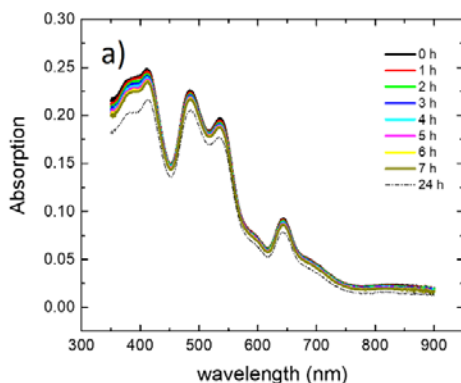

Figure S2. a) UV-vis absorption measurements of IBANs in DMF solution acquired at different times: from 0 (pristine) to 24 hours. Color code: (black) 0h, (red) 1h, (green) 2h, (blue) 3h, (cyan) 4h, (magenta) 5h, (yellow) 6h, (dark yellow) 7h, (dot line) 24h.
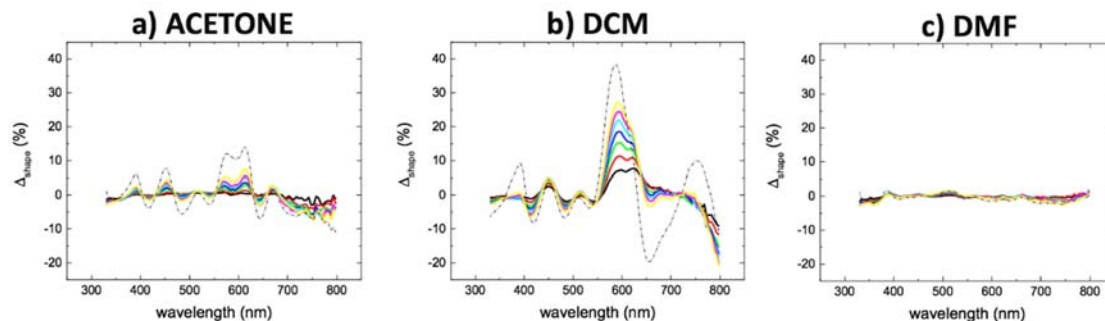

Figure S3. Percentage variation of the spectra acquired in acetone, DCM and DMF during 24 hours. Color code is the same of fig. S2.

Fig. S3 shows the relative changes observed for IBAN in the three solvents, measured as Δ_{shape}. In the case of acetone, the line-shape difference amount to ca 7% indicating that the presence in solution of both pristine IBAN and modified nanoparticles.

For DCM, Δ_{shape} is much higher, up to 40%, indicating a significant degradation of the IBAN already in solution.

As a reference, we also tested a solvent for which changes are minimal, i.e. dimethylformamide (DMF). In DMF, the absolute value <A> decreases of ca 20% in 24 hours while the line-shape variation is <3% respect to the absorption spectrum acquired on the pristine solution (0 h). Being $\Delta_{shape} \approx 0$, the UV-vis measurements clearly shows that more than 97% of nanoparticle in solution are IBAN within the first 24 hours (more than 98% within the first 8 hours corresponding to the SVA time).

Re-Dissolution of C_1 single mesoscopic crystals in acetone

SVA in acetone gave a great number of mesoscopic C_1 crystals. We manually removed one of these C_1 crystal (fig. S4a), analyzed it by XRD and re-dissolved it in acetone solvent, to demonstrate that it was composed by pristine IBAN.

The new solution obtained did no show Tyndall effect or the presence of precipitates visible by eye, and as well as that the UV-vis absorption spectra measured on the obtained solution clearly showed the five features observed in the pristine solution, as depicted in figure S4.
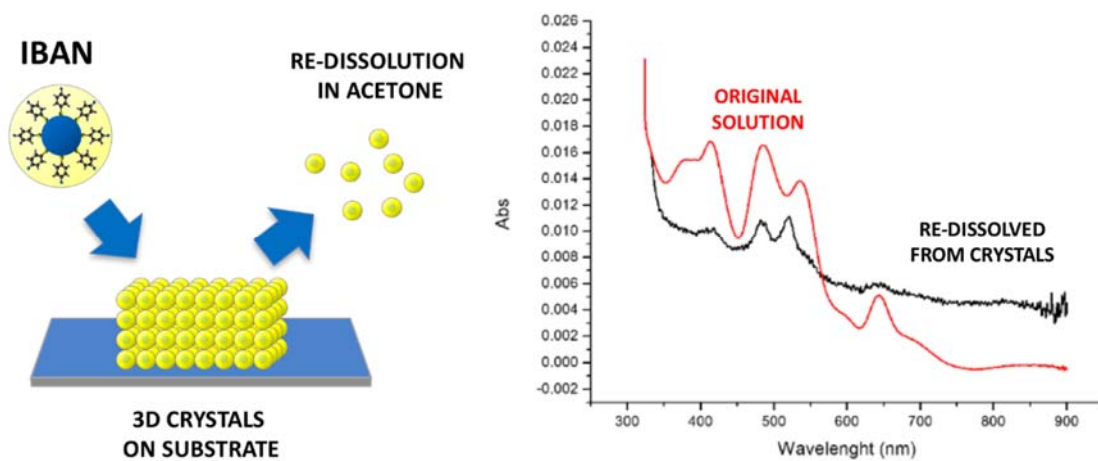
Figure S4. Scheme of the process used to confirm the stability of IBAN in C_1 structures. UV-vis absorption spectra acquired on acetone solution before the SVA treatment (red) and after the dissolution of the C_1 crystal in acetone (black).
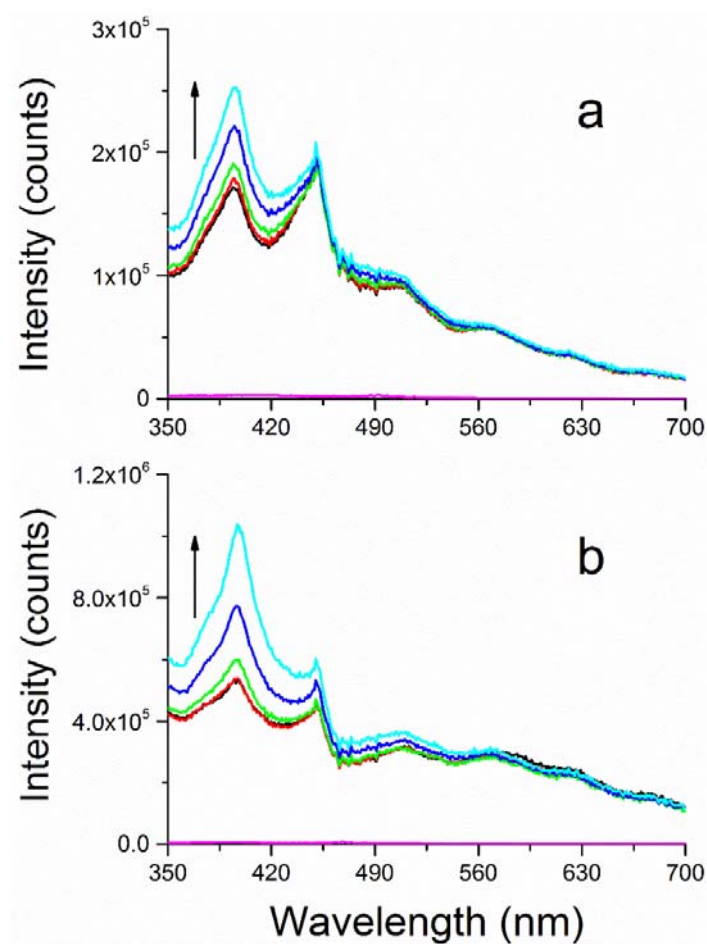
Figure S5. Time evolution of the RLS spectra of IBAN solutions in acetone (a) and DCM (b), recorded at RT over a 24 hour period. The RLS spectra of each solvent (magenta) are reported for comparison.

The intensity of the Resonance light scattering spectroscopy (RLS) spectra of freshly prepared IBAN solutions in acetone and DCM was about 70-fold higher than that of both neat solvents spectra (Fig. S5), in line with the presence of noble metal nanoparticles in solution.[1] In time, both IBAN solutions displayed an increase in the intensity of the scattered light, these phenomena being more prominent in DCM, indicating the growth of aggregated species.

XPS/Auger measurements

XPS analysis performed on the IBANs (wide spectrum in fig. S6c) confirms the presence of the atomic species: Ag, F, C and S. Because of the XPS spectrum of the ligand is currently not available in literature, we assume that the electronic properties of the 4FTP are similar to the Florobenzene[2] and the Thiopenol,[3] as confirmed by measured binding energies (B.E.) in good agreement with the values reported in literatures. C 1s (285.5 ± 0.1 eV) is compatible with C 1s emission in Fluorobenzene (285.5 ± 0.4 eV); F 1s (687.6 ± 0.1 eV) is compatible with a C-F bond, i.e. Poly(vinyldene fluorinde) (688.1 ± 0.3 eV),[4] while the S $2p_{3/2}$ (162.9 ± 0.1 eV) has a similar energy position of the Thiopenol (163.3 eV).[3]
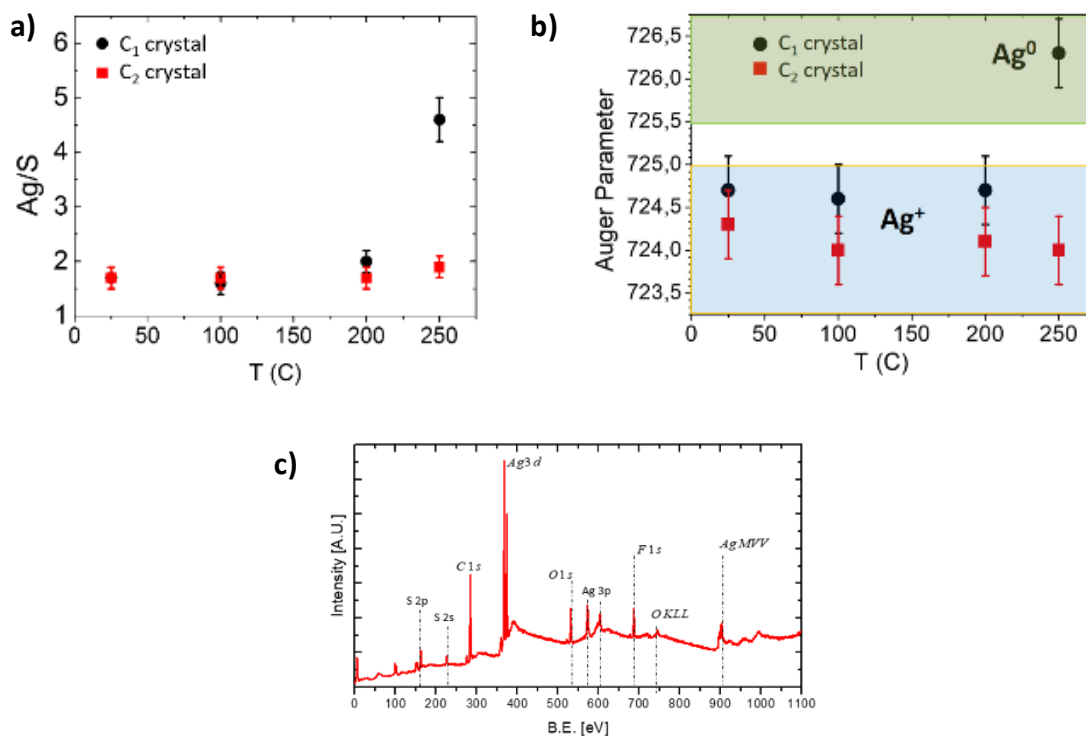

Figure S6. a) Ratio between Silver and Sulfur atoms, as measured by XPS spectra and b) Auger parameters measured at different annealing temperature, from RT to 250 °C. c) XPS spectrum of IBANs.

We analyzed both photoelectron and Auger peak positions, the Auger modified parameter[5] being very sensitive to the chemical state. In the case of silver, the measured B.E. of the Ag $3d_{5/2}$ (368.8±0.1 eV) and the Auger parameter (AP-$3d_{5/2}$, $M_4N_{45}N_{45}$ = 724.7±0.4 eV) can be unambiguously attributed to a non-metallic Silver being 368.7±0.1 (Ag^+) eV and AP-$3d_{5/2}$, $M_4N_{45}N_{45}$ is the range 723.0-724.9 eV ($Ag^{+/2+}$),[6] respectively.

Thermal annealing – C_1 crystal

The degradation of NP was monitored by looking at the Ag/S ratio. At room temperature the Ag/S ratio was 1.7±0.2 (Table S1), compatible with the stoichiometric ratio (Ag/S = 1.47).

T [C]	Ag/F	Ag/S	S/F	Auger modified parameter
25	2.1 ± 0.3	1.7 ± 0.3	1.2 ± 0.3	724.7 ± 0.4
100	2.3 ± 0.2	1.6 ± 0.4	1.4 ± 0.3	724.6 ± 0.5
200	2.9 ± 0.2	2.0 ± 0.2	1.4 ± 0.3	724.7 ± 0.8
250	7.4 ± 0.2	5.4 ± 0.4	1.4 ± 0.5	726.3 ± 0.3

Table S1. C_1 crystals. Atomic species ratio, as measured by XPS at different annealing temperature.

By heating up to 250°C, C_1 crystals began to melt following the desorption of ligands, as observed by Mass Spectroscopy. In particular, we used the Auger spectroscopy analysis to monitor the chemical state of silver atoms (figure S5b) at increasing temperature. Auger parameter AP-$3d_{5/2}$, $M_4N_{45}N_{45}$ remains constant in the non-metallic Ag region until 250° C, confirming the Ag^+ state at low temperature, due to the confinement in the nanometric core and as well as the Ag-S bond. Only at 250 °C, a difference was observed (Ag^0) with a corresponding transition to metallic silver strongly indicating the melting of the IBAN nanoparticles. The measured Binding Energy of Ag $3d_{5/2}$ (368.1±0.1 eV) is in good agreement with the expected

B.E. value for bulk (368.20-368.30 eV) and in excellent agreement with the reported value for the Ag metallic nanoparticle (368.1±0.1 eV).[7]

Thermal annealing – C$_2$ layered crystal

XPS analysis performed on C2 layered structures (see table S5) showed the same chemical composition and electronic structure of the NP in the C$_1$ crystals: S/F and Ag/S ratios were respectively 1.2±0.2 and 1.7±0.2; also the Ag was in non-metallic state, as observable from Auger parameter AP-3d$_{5/2}$, M$_4$N$_{45}$N$_{45}$ equal to 724.3±0.5 eV (see Fig. S3).

T [C]	Ag/F	Ag/S	S/F	Auger modified parameter
25	2.1 ± 0.2	1.7 ± 0.2	1.2 ± 0.2	724.3 ± 0.5
100	2.0 ± 0.2	1.7 ± 0.2	1.2 ± 0.2	724.0 ± 0.5
200	2.0 ± 0.2	1.7 ± 0.2	1.2 ± 0.2	724.1 ± 0.5
250	2.0 ± 0.2	1.9 ± 0.2	1.1 ± 0.2	724.4 ± 0.8

Table S2. C$_2$ crystals. Atomic species ratio, as measured by XPS at different annealing temperature.

Clustering in acetone solution

AFM measurements

IBAN were fairly stable in acetone, as monitored during the first 24 hours. For longer time, layered structures were also found in acetone solutions.

A drop of aged solution (3 weeks) was spun on silicon oxide. The acquired AFM images (fig. 7) showed the presence of aggregates of 2D sheets having similar lateral size (ca 500 nm) and thickness (ca 2 nm). Moreover, the interfacial angle of the 2D sheets amounted to ca 55°, in good agreement with AFM and GIWACS measurements (see table 1 in main text).

AFM images suggested that the observed 2D sheets are formed by C_2 layered structures.
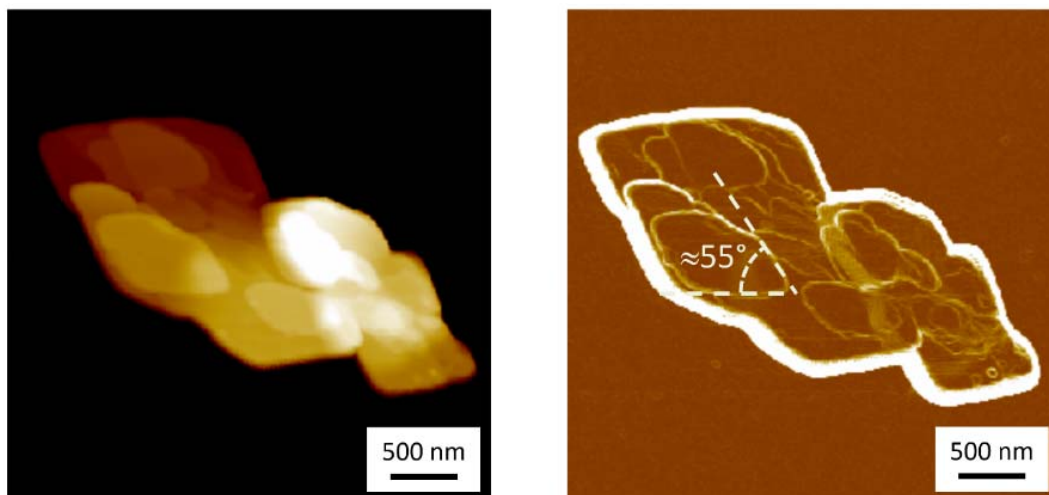

Figure S7. Topographic (left) and corresponding gradient (right) AFM image of clusters deposited on native silicon oxide. Acetone solution few-days old. Z-range: (a) 60 nm.
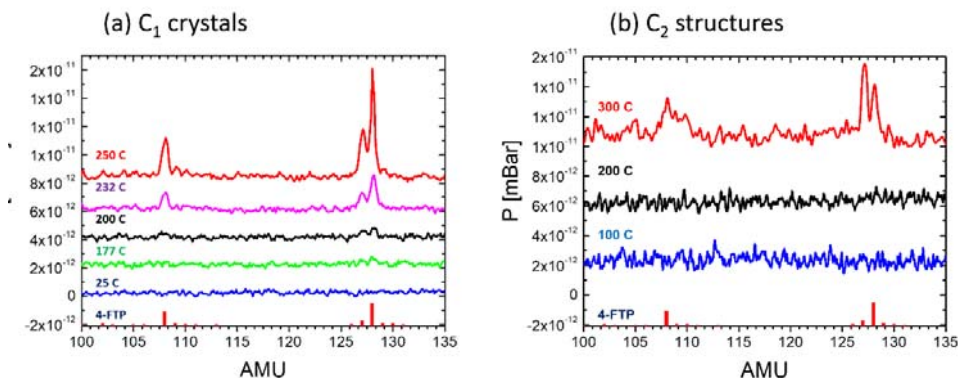
RGA analysis

Figure S8. Mass spectra acquired during RGA at different temperatures on (a) C_1 crystals and (c) C_2 structures. RGA spectra of pure 4-FTP ligand (red columns in the lower part of the graphs) are shown as reference.

IBAN decomposition started for T>170°C, as observed by optical spectroscopy, XRD (fig. S6) and residual gas analysis (RGA, fig. S8); I*n-situ* XPS analysis during thermal treatments in UHV showed that 4-FTP molecule does not degrade up to 300°C: the S/F ratio remained constant within experimental error (Table S1,S2), while a desorption phenomenon was observed by the decrease of S or F respect the Ag, which gave an increase of the Ag/S ratio from 200 °C. A more accurate evidence of desorption dynamics was given by Mass Spectroscopy, the 4-FTP molecule, identified by m/z = 128, $FC_6H_4SH^+$, 127 $FC_6H_4S^+$ and 108 $C_6H_4S^+$, was desorbed from the IBAN at T> 170°C (fig. S8 (a)). Literature data report a similar desorption temperature (187 °C) for 4-FTP on Au (SEM).[8]
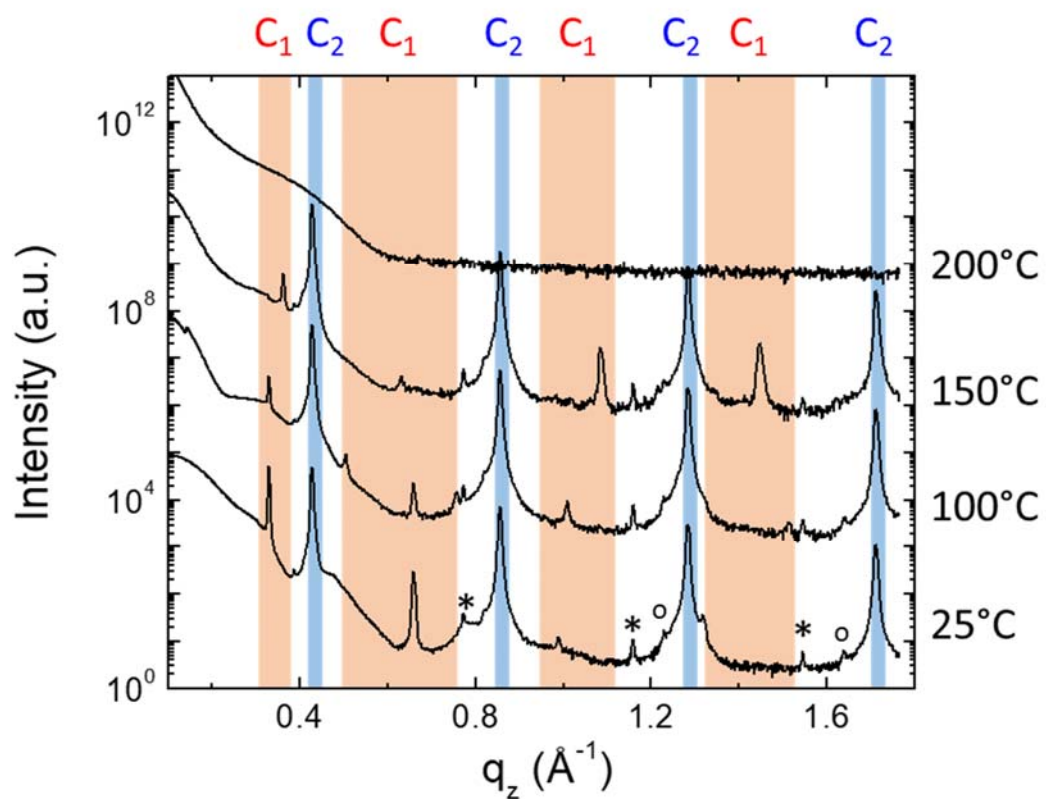
Figure S9. Specular XRD measurements acquired at different annealing temperatures on C_1 and C_2 crystals of IBAN obtained by SVA in acetone. Features marked in orange boxes are ascribable to C_1 crystals. Asterisks and empty dots indicate peaks of the C_2 crystals from spurious wavelengths (Cu Kβ and W Lα).
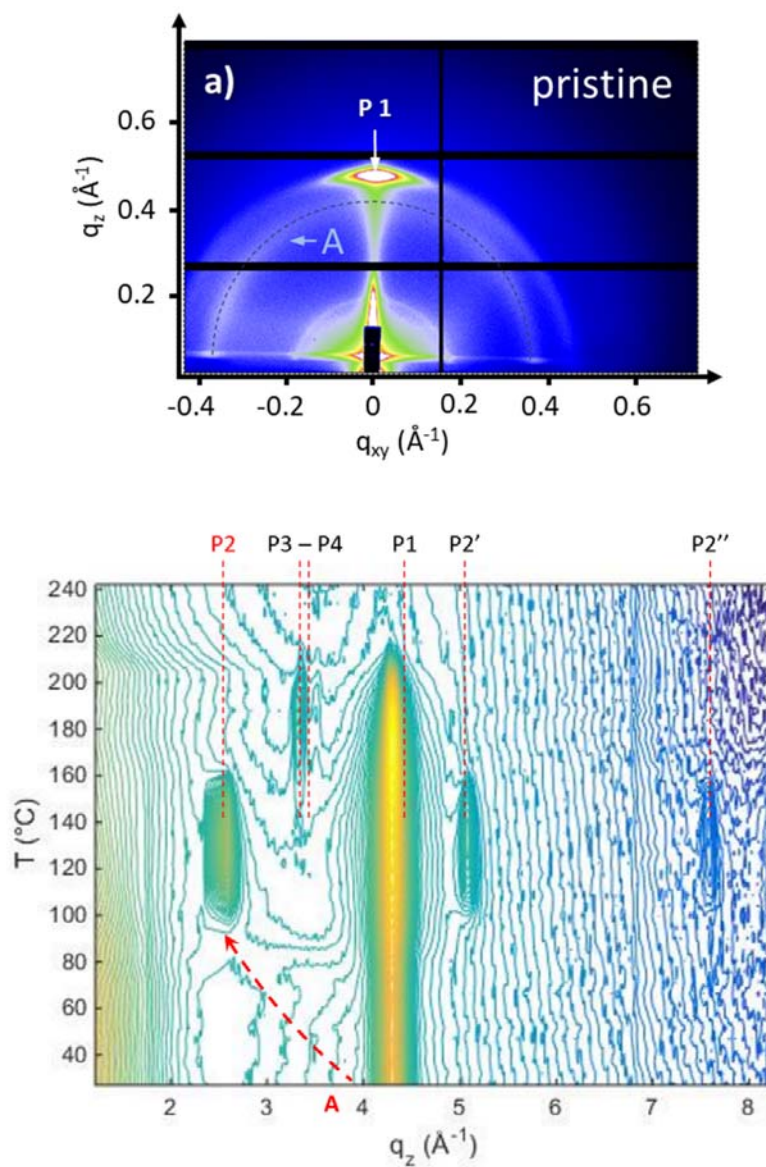
SVA in DMF, monitored in-situ by GISAXS

Figure S10. a) GISAXS of C_1 and C_2 crystals of IBAN obtained by SVA in acetone, before annealing. b) Intensity integrated along the out-of-plane direction of GISAXS images collected in-situ and real time during thermal annealing.

Figure S10 represented the same data shown in fig. 7 in main text, but plotted as 2D graph with level curves. The chosen visualization allowed to clarify the nature of P2 peak which can be

assigned to the re-organization of aggregates of IBAN (labelled with A and corresponding to the ring in 2D-GIWAXS image in fig. 6).
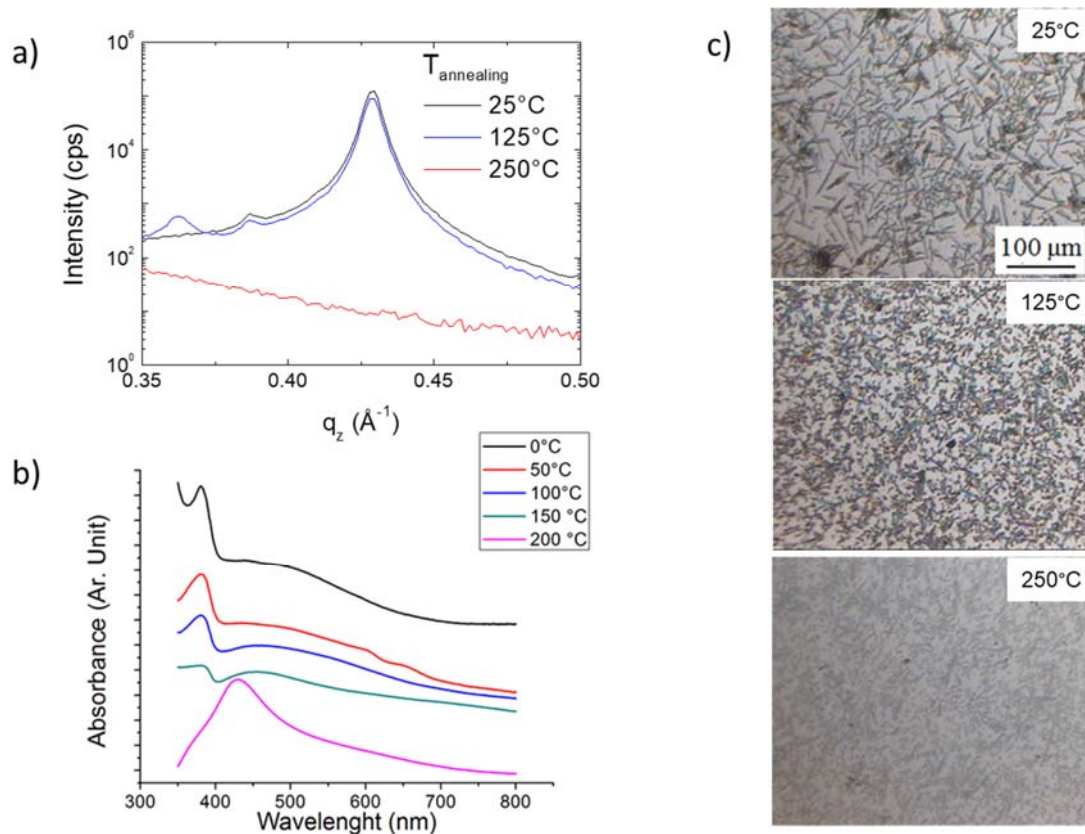

Figure S11. Characterization at different temperatures of C_2 crystals of IBAN obtained by SVA in DCM. (a) XRD patterns, (b) UV-vis absorption of C_2 layered structures on quartz substrates and (c) corresponding optical images.

GIWAXS measurements

GIWAXS analysis of IBAN structures obtained by SVA in acetone (Fig. S12a-b) revealed the coexistence of both C_1 3D lattices and C_2 layered structures. While the Bragg spots evidenced by red arrows and ovals came from the C_2 structure, the most intense and narrow spots came from the C_1 structure of NPs superlattices. For this latter, the position and intensity of Bragg spots can be explained by assuming that crystals grow mainly having [001] texturing and were randomly oriented in-plane. The simulation of the Bragg spots of C_1 structure in the small angle region is reported in Fig. 2c. The appearance and disappearance of Bragg spots in GIWAXS images, when collected at different positions, arose from the absence of all the possible in-plane orientations of single-crystals.
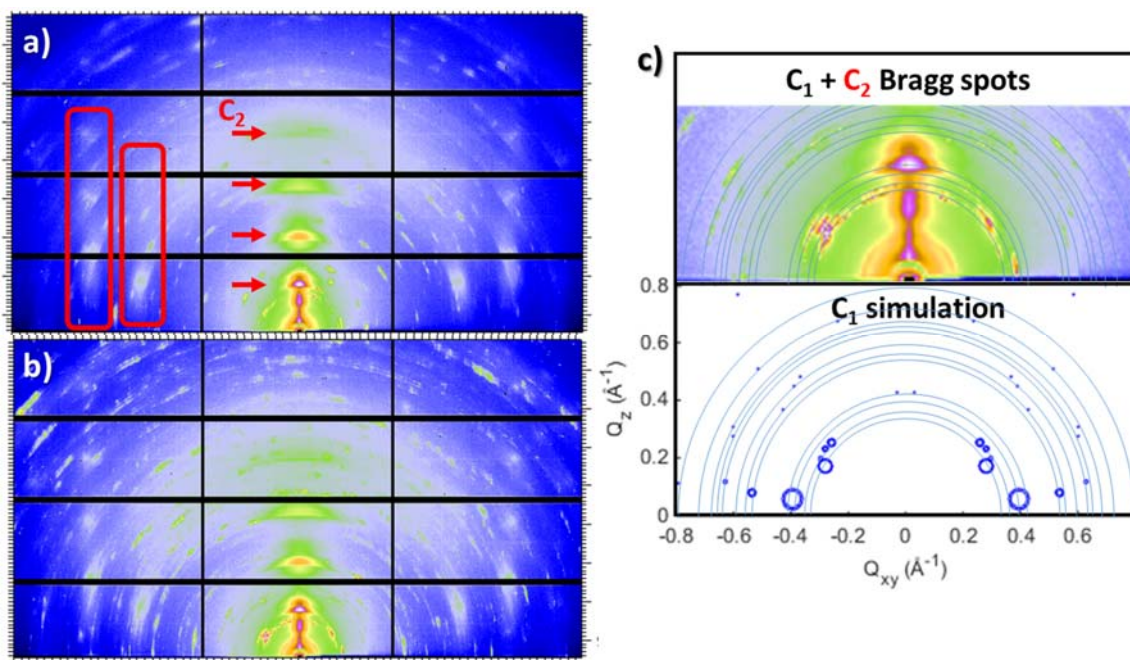

Figure S12. (a-b) 2D-GIWAXS image of IBAN structures formed by SVA in acetone recorded at different position of the substrate. The Bragg spots coming from the C_2 structures are highlighted by red lines and rectangles only in the first image. c) Calculated positions of Bragg peaks, in the small angles region of the reciprocal space, from the C_1 structure of NPs crystals assuming a [001] texturing and a random orientation in the plane parallel to the surface. The areas of the circles are proportional to

the peak intensity. Circles are also plotted to show the Bragg spots' position in the case of random grain orientation.

Single-crystal X-ray diffraction analysis of C_1 crystals

XRD measurements were performed at two temperatures, room temperature (RT, 298 K) and high temperature (HT, 400 K), as reported in Table S3. C_1 crystal showed a triclinic structure with a high-density packing of IBANs, as depicted in fig. 4 in main text. Crystallographic asymmetric units (ASUs) show half IBAN, since an inversion center lays in the barycenter of each silver cluster (Fig. S13-S14).

We observed the same crystal packing at both 298 K, and 400 K, with a volume expansion upon heating of 5.7% and minor organic residues rearrangements. Root-mean-square deviation between models calculated at both temperatures was 2.9 Å. **C_1** crystals showed a high-density packing of IBANs, as depicted in fig. S16, held together by hydrophobic interactions among the organic ligands on the clusters surfaces. Tetraphenyl- phosphine counterions were housed in between the nano–particles, neutralizing the net negative IBAN charges ($[Ag_{44}(SPhF)_{30}][P(Ph)_4]_4$).

The residual empty volume, corresponding to ~3% of the unit cell, is divided into small cavities of ~40 $Å^3$ each. The Kitaigorodskii packing index[9] amounts to ~65% and the poor residual electron density in cell voids ($\approx$10 e$^-$/cell, as calculated from PLATON SQUEEZE[10] routine), strongly suggests that there is no solvent inside this IBANs polymorph.

The SVA crystallization procedure led to a new triclinic crystal form for $[Ag_{44}(SPhF)_{30}]^{4-}$, significantly different from previously published one,[11] as an effect of the different protocol used. Fig. S16 shows the packing of IBAN obtained by SVA in acetone in this work; Figure S17 shows the packing published in previous works[11] for IBAN with the same Ag_{44} cluster and similar side groups (SPhF), yielding a cell with a volume double respect to the previously

known crystal form[11] (volumes reported in captions on Figure S16 e S17). Noteworthy, the C_1 crystal structure obtained by SVA in acetone was similar to the one of $Au_{12}Ag_{32}$ equivalent crystals (fig. S18) previously published[11]. Despite similar intercluster distances ($D_{crystal} \approx 20$ Å) and similar arrangement of organic residues, among all structures, the crystal packing of previously determined polymorphs show ~15% of cavities containing disordered solvent molecules.

In C_1 crystal, the distances between IBAN were smaller than IBAN diameter: $D_{crystal} < D_{IBAN}$, due to the interdigitation of ligands. We define the effective radius as half the distance between two nanoparticles: $R_{eff} = D_{crystal}/2$. R_{eff} corresponded to the radius of NPs using the rigid spheres model amounting to ≈ 10 Å.

Distances and geometrical displacements measured by single crystal XRD corresponded to the values: $R_{eff}/R_{core} \approx 1.6$ and $l_{ligand}/R_{core} \approx 0.9$. These two values are in excellent agreement with the description obtained by the Optimal Packing Model (OPM)[12] which postulated that the space-filling of ligands is placed along the axis between the two cores.
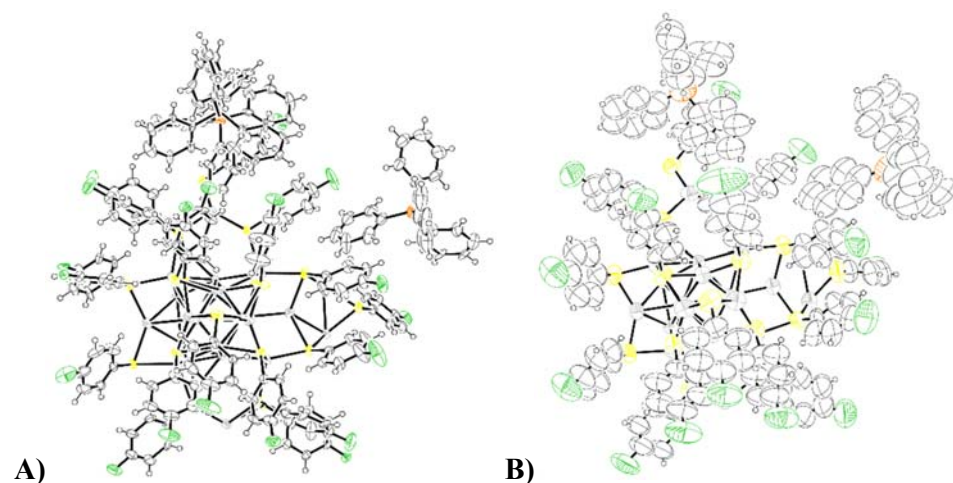

A)   B)

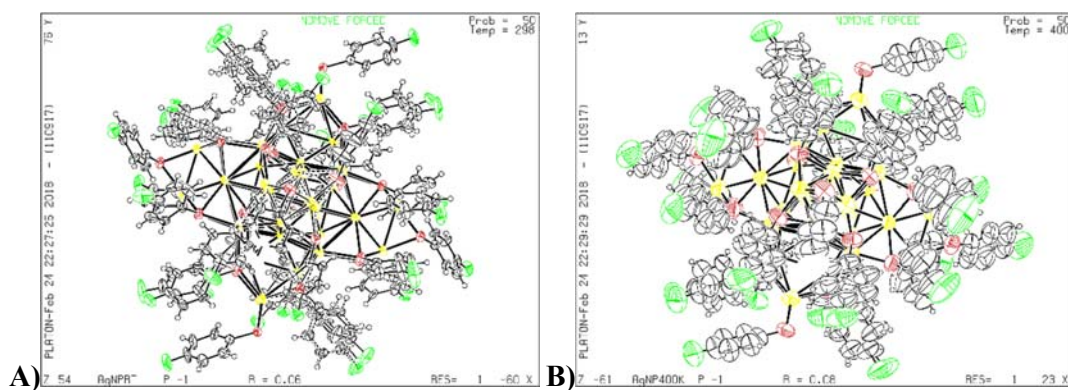**Figure S13.** Ellipsoids representation of ASU contents (50% probability) for: A) C_1^{RT} and B) C_1^{HT}.

Figure S14. Ellipsoids representation of the complete Ag44 nanoparticles (50% probability) for: A) C_1^{RT} and B) C_1^{HT}.
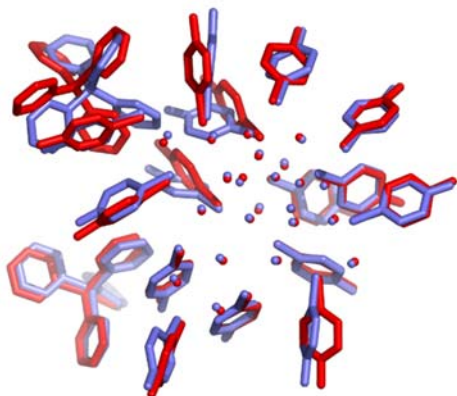

Figure S15. Superimpositon of C_1^{RT} and C_1^{HT} ASU contents: the 298K and 400K are represented with blue and red sticks, respectively. Hydrogens and disordered conformations are omitted for clarity.
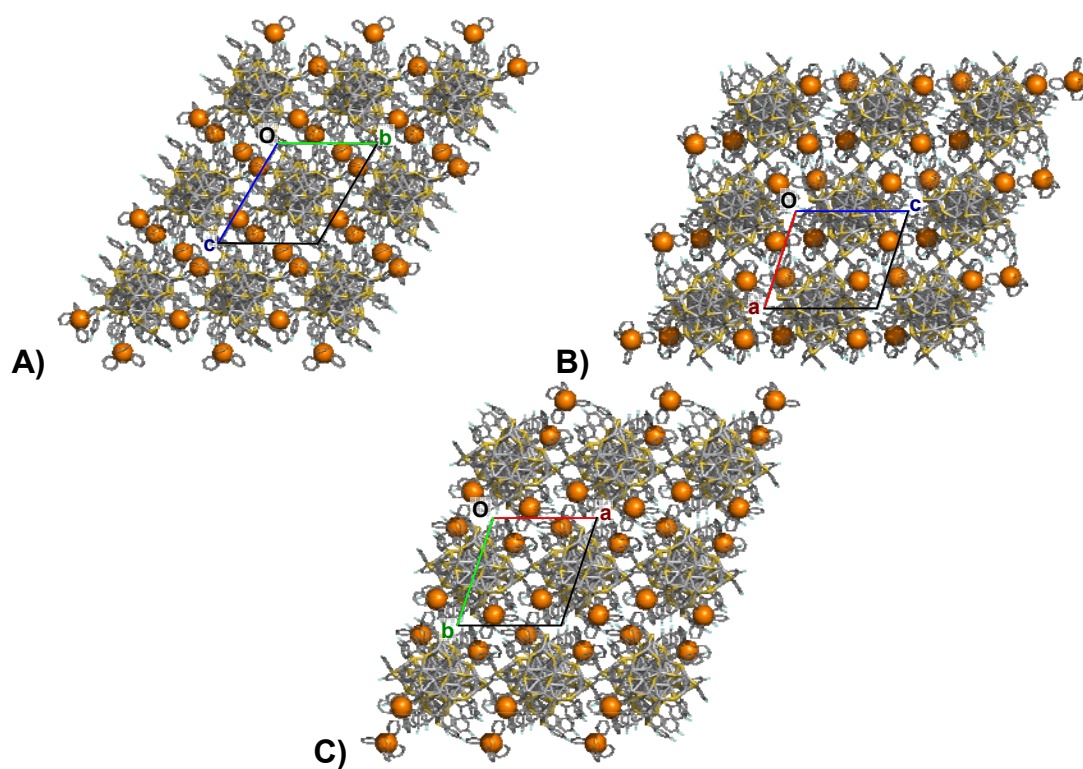
Figure S16. Crystal packing views of [Ag$_{44}$(SPhF)$_{30}$][P(Ph)$_4$]$_4$ new crystal form (this work), along crystallographic *a*, *b* and *c* directions (Cell parameters at 298K: *a*=20.4051(4) Å, *b*=20.8665(4) Å, *c*=21.9791(4) Å, α=114.956(2)°, β=93.756(2)°, γ=116.423(2)°; corresponding cell at 400K: *a*=20.901(4) Å, *b*=21.475(4) Å, *c*=22.624(18) Å, α=115.62(3)°, β=93.93(4)°, γ=117.69(3)°; Space Group: *P*-1; Volume≈7,425 Å^3). P atoms are represented as spheres, while the metallic clusters are shown as sticks.

Figure S17. Crystal packing views of $[Ag_{44}(SPhF)_{30}][P(Ph)_4]_4$ crystal form already published[11] along crystallographic a, b and c directions (Cell parameters: a=20.6535(5) Å, b=21.7398(5) Å, c=37.0707(6) Å, α=76.0130(17)°, β=82.9775(16)°, γ=71.728(2)°; Space Group: P-1; Volume=15317.4(5) Å^3). The blue stars show the position of voids containing squeezed solvent electrons at (0, 0, 0). P atoms are represented as spheres, while the metallic clusters are shown as sticks.

Figure S18. Crystal packing views of $[Au_{12}Ag_{32}(SPhF)_{30}][P(Ph)_4]_4$ crystal form already published[11] along crystallographic *a*, *b* and *c* directions (Cell parameters: *a*=20.5841(5) Å, *b*=21.7003(6) Å, *c*=21.9350(6) Å, α=67.617(3)°, β=63.981(3)°, γ=71.534(2)°; Space Group: *P*-1; Volume=8,008.4(4) $Å^3$). The blue stars show the position of voids containing squeezed solvent electrons at (0, 0, 1/2). P atoms are represented as spheres, while the metallic clusters are shown as sticks.
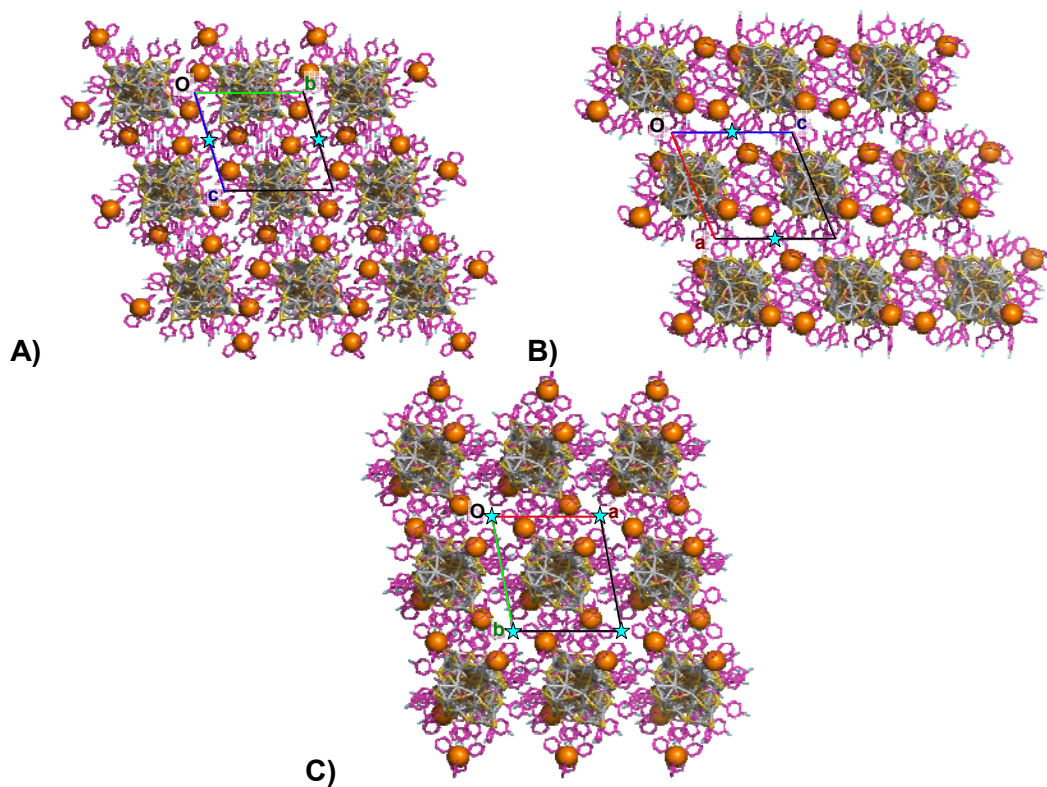
	C_1^{RT}	C_1^{HT}
	$[Ag_{44}(C_6H_4FS)_{30}](C_{24}H_{20}P)_4$	$[Ag_{44}(C_6H_4FS)_{30}](C_{24}H_{20}P)_4$
CCDC Number	1830015	1830014
Chemical Formula	$C_{276}H_{200}Ag_{44}F_{30}P_4S_{30}$	$C_{276}H_{200}Ag_{44}F_{30}P_4S_{30}$
Formula weight (g/mol)	9918.31	9918.31
Temperature (K)	298(2)	400(2)
Wavelength (Å)	0.70848	0.700
Crystal system	Triclinic	Triclinic
Space Group	P -1	P -1
Unit cell dimensions*	$a = 20.4051(4)$ Å	$a = 20.901(4)$ Å
	$b = 20.8665(4)$ Å	$b = 21.475(4)$ Å
	$c = 21.9791(4)$ Å	$c = 22.535(5)$ Å
	$\alpha = 114.956(2)°$	$\alpha = 95.04(3)°$
	$\beta = 93.756(2)°$	$\beta = 114.57(3)°$
	$\gamma = 116.423(2)°$	$\gamma = 117.69(3)°$
Volume (Å^3)	7219.0(3)	7632(4)
Z	1	1
Density (calculated) (g·cm^{-3})	2.281	2.158
Absorption coefficient (mm^{-1})	3.139	2.875
F(000)	4734	4734
Crystal size (mm^3)	0.10 x 0.05 x 0.03	0.10 x 0.05 x 0.03
Crystal habit	Thick black prisms	Thick black prisms
Theta range for data collection	1.78° to 24.32°	1.04° to 24.30°
Resolution (Å)	0.86	0.85
Index ranges	-23 ≤ h ≤ 23	-24 ≤ h ≤ 24
	-24 ≤ k ≤ 24	-25 ≤ k ≤ 25
	-25 ≤ l ≤ 25	-26 ≤ l ≤ 26
Reflections collected	77038	64828
Independent reflections (data with I>2σ(I))	22412 (15408)	25167 (15105)
Data multiplicity (max resltn)	3.24 (3.07)	2.50 (2.22)
I/σ(I) (max resltn)	7.11 (3.67)	7.82 (2.30)
R$_{merge}$ (max resltn)	0.0937 (0.1996)	0.0527 (0.3285)

Data completeness (max resltn)	94.3% (91.8%)	96.9% (94.6%)
Refinement method	Full-matrix least-squares on F^2	Full-matrix least-squares on F^2
Data / restraints / parameters	22412 / 727 / 1886	25167 / 1098 / 1454
Goodness-of-fit on F^2	1.029	1.060
Δ/σ_{max}	0.006	0.009
Final R indices [$I>2\sigma(I)$][a]	$R_1 = 0.0585$, $wR_2 = 0.1333$	$R_1 = 0.0773$, $wR_2 = 0.2195$
R indices (all data)[a]	$R_1 = 0.0880$, $wR_2 = 0.1459$	$R_1 = 0.1250$, $wR_2 = 0.2602$
Largest diff. peak and hole (e·Å^{-3})	1.344 and -1.642	1.269 and -0.958
R.M.S. deviation from mean (e·Å^{-3})	0.195	0.180

[*]**C$_1$**^{RT} and **C$_1$**^{HT} unit cells shown are reduced forms and can be lead to the same axis choice applying the following transformation: {-1.0 0.0 0.0, 0.0 -1.0 0.0, 1.0 1.0 1.0}

[a] $R_1 = \Sigma \, ||F_o|-|F_c|| \, / \, \Sigma \, |F_o|$, $wR_2 = \{\Sigma \, [w(F_o^2 - F_c^2)^2] \, / \, \Sigma \, [w(F_o^2)^2]\}^{1/2}$

Table S3. Crystallographic data and refinement details for **C$_1$**^{RT} and **C$_1$**^{HT}.
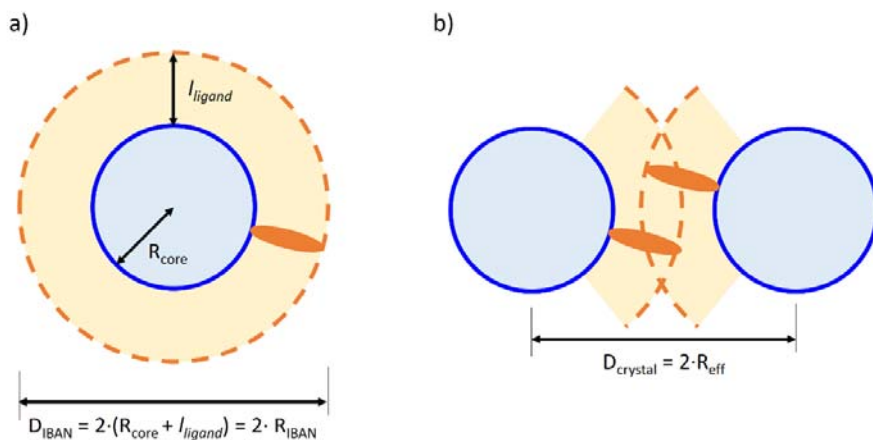
Figure S19. Packing of ligands in C_1 superlattices. Sketches of (a) single IBAN and (b) interdigitating ligands coronas between two IBANs showing core radius R_{IBAN}, ligand length l_{ligand}, and effective radius R_{eff}.

	Value (Å)		Value (Å)
R_{core}	6.5	D_{IBAN}	24.8
l_{ligand}	5.9	R_{IBAN}	12.4
$D_{crystal}$	20	R_{eff}/R_{core}	≈ 1.6
R_{eff}	10	l_{ligand}/R_{core}	≈ 0.9

Table S4. Summary table of the distances and dimensions of IBANs arranged in the C_1 crystal.

DFT calculation for C₂ crystal

The molecular packing of the 2D structures obtained by decomposition of the IBAN was determined by optimizing a handful of trial structures, generated with the program GDIS[13] matching the experimentally determined crystal cell. Each structure was first optimized by keeping constant the cell, followed by a second optimization with this constraint removed. The crystal structures obtained were ranked by their relative energy, which never exceeded 10 kcal/mol. The best structure was determined by comparison with the XRD data. The results obtained indicate thus that, with simple exposure to DCM solvent, the silver atoms undergo an oxidative transformation, losing the stability given by the "magic number" 18 electrons closed shell and transforming into a layered structure in which two Ag atoms maintain their formal oxidation state, while one atom of Ag is in a formal neutral state.
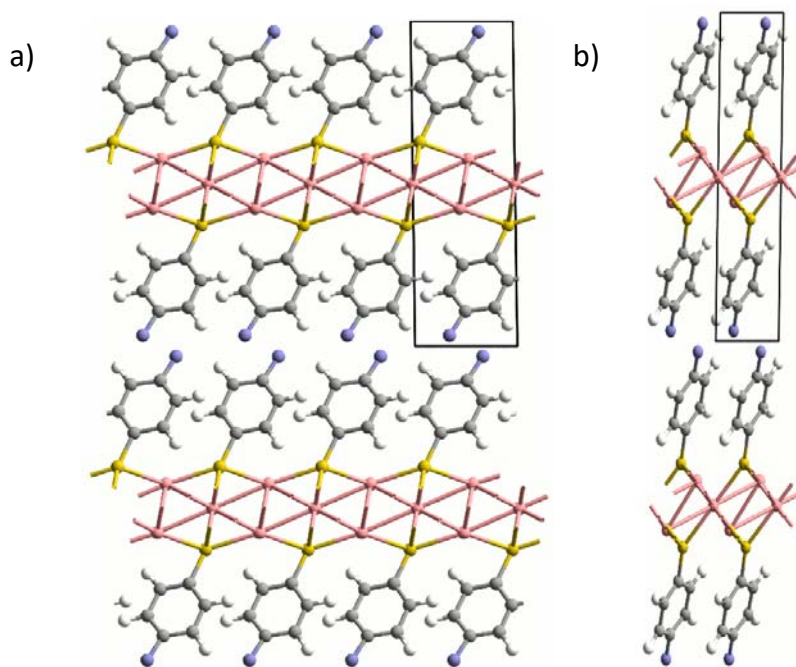

Figure S20. Structure of C₂ crystal along the planes generated by vectors: a) a,c and b) b,c. Ag atoms are in silver color, S in yellow, C in dark grey, H in light gray, F in green.

Qualitative analysis of MFM images

Maps of the magnetic field of the samples were obtained by magnetic force microscopy (MFM) performed with a Smena Head microscope (NT-MDT, Russia). Magnetic cantilevers with resonance frequency of about 75 kHz, coated with a cobalt/chromium magnetic layer, were used (Multi75M-G BudgetSensors, Bulgaria). An external magnetic field was applied to both sample and tip (for few seconds) in order to enhance their magnetization. All samples were topographically imaged by using AFM intermittent contact mode, while MFM images were collected in lift mode at fixed distance (50 nm).

MFM images of C_1 and C_2 show a contrast due to different magnetic interaction between the cantilever tip and the sample, causing a shift in the phase of the oscillating tip (set to 0° for null magnetic field).[14]

After SVA in acetone (fig. S21a,b), both C_1 (marked by box) and C_2 crystals were observed. As shown in Figure S21b, most of C_2 crystals show magnetic contrast composed of small regions with positive contrast – brighter contrast – with respect to large regions with negative one – darker contrast – (see false color scale bars). The measured shift are not due to experimental artefacts, as verified by varying the scanning direction of the tip, and strongly indicates the paramagnetic behaviour of C_2 crystals. Fixed the magnetization moment of the tip vertically respect to the surface sample (up or down[15]), the corresponding average direction of the magnetization moment of the sample can be parallel (antiparallel) respect to the tip, being an attractive (repulsive) interaction and corresponding to a negative(positive) shift of the phase signal. Conversely, the magnetic contrast of C_1 crystals is quite negligible, indicating diamagnetic properties, as observed for the silicon substrate.

After SVA in DCM (fig. S21c,d) only C_2 crystals were observed. As expected, they show the paramagnetic behaviour (dark regions), similar to the one observed for crystals obtained in acetone. Interestingly, some crystals show areas with neglegible phase contrast, as measured

on the substrate. This effect can be ascribible to the presence of IBAN assemblies (nanometric thick) grown on C_2 crystals surfaces. The diamagnetic behavoiur of such assemblies hinders the magnetic contrast of the underlying crystals.
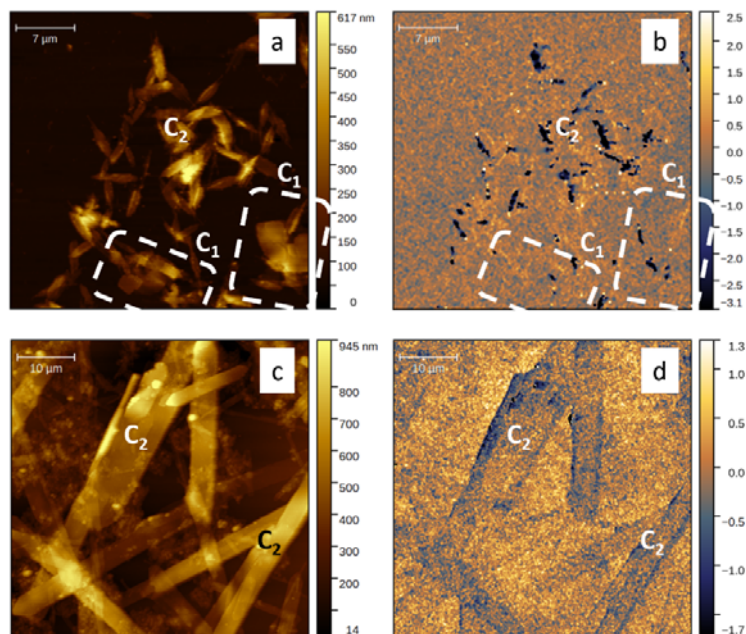

Figure S21: Topographic (a, c) and MFM (c, d) images of C_1 and C_2 crystals.

Bibliography

1. N. Micali, F. Mallamace, M. Castriciano, A. Romeo and L. Monsú Scolaro, *Analytical Chemistry*, 2001, **73**, 4958-4963.
2. D. T. Clark, D. Kilcast and W. K. R. Musgrave, *Journal of the Chemical Society D: Chemical Communications*, 1971, DOI: 10.1039/C2971000516B, 516b-518.
3. B. J. Lindberg, K. Hamrin, G. Johansson, U. Gelius, A. Fahlman, C. Nordling and K. Siegbahn, *Physica Scripta*, 1970, **1**, 286.
4. H. Hantsche, *Advanced Materials*, 1993, **5**, 778-778.
5. S. W. Gaarenstroom and N. Winograd, *The Journal of Chemical Physics*, 1977, **67**, 3500-3506.
6. A. M. Ferraria, A. P. Carapeto and A. M. Botelho do Rego, *Vacuum*, 2012, **86**, 1988-1991.
7. F. Benedetti, P. Luches, M. C. Spadaro, G. Gasperi, S. D'Addato, S. Valeri and F. Boscherini, *The Journal of Physical Chemistry C*, 2015, **119**, 6024-6032.
8. H. Kang, E. Ito, M. Hara and J. Noh, *Journal of Nanoscience and Nanotechnology*, 2016, **16**, 2800-2803.
9. A. I. Kitaigorodskii and C. Bureau, 1961.
10. A. L. Spek, *Acta Crystallographica Section C: Structural Chemistry*, 2015, **71**, 9-18.
11. H. Y. Yang, Y. Wang, H. Q. Huang, L. Gell, L. Lehtovaara, S. Malola, H. Hakkinen and N. F. Zheng, *Nature Communications*, 2013, **4**, 8.
12. U. Landman and W. D. Luedtke, *Faraday Discussions*, 2004, **125**, 1-22.
13. S. Fleming, *Journal*.
14. U. Hartmann, *Annual Review of Materials Science*, 1999, **29**, 53-87.
15. L. Kong and S. Y. Chou, *Applied Physics Letters*, 1997, **70**, 2043-2045.